# Ritchey–Common sparse-aperture testing of the Giant Steerable Science Mirror

QICHANG AN,[1,2] JINGXU ZHANG,[1] FEI YANG,[1] HONGCHAO ZHAO,[1,*] AND HAIFENG CAO[1,2]

[1]*Changchun Institute of Optics, Fine Mechanics and Physics, Chinese Academy of Sciences, Changchun 130033, China*
[2]*Graduate University of Chinese Academy of Sciences, Beijing 100039, China*
*Corresponding author: zhaohcciomp@163.com*

The Giant Steerable Science Mirror (GSSM) is the tertiary mirror of the future large telescope, the Thirty Meter Telescope. However, the mirror is too large to be tested using only one aperture, and using many apertures will increase the cost of testing. To accomplish testing at a low cost, the number of apertures should be reduced. The Ritchey–Common (R–C) testing method, commonly used for testing large flat surfaces, uses only a reference spherical mirror and avoids the use of large planar interferometers. Additionally, only the low-spatial-frequency mirror figure is relevant in the system assembly and alignment. Hence, the applicability of sparse-aperture testing is investigated in this paper. Sparse-aperture testing and the R–C method were combined to lower the cost. Using this method and the normalized point source sensitivity (PSSn), the mirror figure can be specified in a simple and accurate manner. Moreover, as fewer subapertures are under test, the efficiency can be improved. An error analysis is conducted, focusing on the shifting error, irregularity error, tipping error, tangential/sagittal error, and seeing. For the testing of the GSSM prototype, the error analysis showed the total error in PSSn is 0.9701. © 2018 Optical Society of America

## 1. INTRODUCTION

Researchers are developing increasingly larger telescopes in order to explore more details of the universe. However, as the size of the planar mirror in the optical system increases, the requirements for large planar mirror testing become more challenging. The Ritchey–Common (R–C) method, which focuses on the measurement of standard planar mirrors, was proposed in 1904 by Ritchey, based on Common's work. Since a planar mirror has no light-focusing function, it needs to be armed with a standard spherical mirror. Because of the relatively low cost of large spherical mirrors, the R–C method can be implemented more easily than large planar interferometer testing [1–6]. The R–C method is used to obtain the figure of the VLT's tertiary mirror [3]. In the Large Sky Area Multi-Object Fiber Spectroscopic Telescope (LAMOST), the R–C method is used to perform qualitative figure testing of the reflecting correcting mirror hexagonal planar mirror with a 1.1 m diagonal line [7].

Subaperture stitching was originally proposed by Kim and Wyant, in the early 1980s, for testing large mirrors without using an interferometer of the same size. Its basic principle is to obtain the complete surface information, part by part [8–12]. However, although the subaperture stitching algorithm

has the unique benefits of expandable measuring range and high lateral resolution, the number of subapertures increases as the size of the telescope increases. Moreover, subaperture testing needs setup translation changes between different locations; therefore, the process must consider the relative position changes and adjustments, both of which affect the stability and repeatability of the measurements. Thus, much redundant time and personnel costs are incurred in the preliminary testing stage. If the number of subapertures can be reduced reasonably or if they can be separated into sparse subapertures, the detection efficiency can be improved greatly. Xu *et al.* studied the sparse-subaperture testing error of a mirror in high-energy laser weapon systems after surface ring polishing [13]. The error distributions of the large optical components vary greatly with scale, unlike those of the smaller planar mirrors. The error characteristics still require further investigation [14–18].

R–C testing requires a standard sphere. However, for large sizes, a large spherical mirror's grinding, supporting, and real-time monitoring can present a series of practical problems and become important factors restricting the application of the R–C method. Yang took advantage of a standard sphere's elliptic projection on a planar mirror, and improved the R–C method's

measuring range to $\sqrt{2}$ times the standard sphere's diameter by rotating the mirror under test. However, for a bigger flat, this method will not work.

For a larger telescope such as the Thirty Meter Telescope (TMT), whose tertiary mirror is a Giant Steerable Science Mirror (GSSM, 3.594 m × 2.536 m), the normalized point source sensitivity (PSSn) must be introduced in the system engineering to fully evaluate its performance [19–23]. Further investigations on the PSSn for GSSM figure testing will promote the error evaluation significantly. For sparse-aperture testing,

In sparse-aperture testing, the figure error of the optical element and the air turbulence are usually contributors to the stitching error. A smaller and faster reference optical item will reduce the error. The GSSM R–C sparse-aperture testing uses smaller, sparsely located apertures to estimate the PSSn of the GSSM.

During GSSM R–C sparse-aperture testing, the OTF is modulated by the entrance pupil, and the relationship between the PSSn and OTF is shown in Eq. (2),

$$\text{PSSn} = \frac{\iint_{A(f_x, f_y)} |\text{OTF}_e|^2 |\text{OTF}_{t+a+e}|^2 |P(x + \gamma f_x, y + \gamma f_y) P(x - \gamma f_x, y - \gamma f_y)|^2}{\iint_{A(f_x, f_y)} |\text{OTF}_{t+a+e}|^2 |P(x + \gamma f_x, y + \gamma f_y) P(x - \gamma f_x, y - \gamma f_y)|^2}, \tag{2}$$

the main problem lies in the separation of the errors introduced by the mirror and the measurement system aberrations. A reasonable error evaluation criterion can help organize the information and extract the valuable information. The PSSn can directly relate the performance evaluation to the imaging quality and is better than the traditional evaluation indexes (RMS, FWHM, 80% EE, etc.) in terms of representing the error in sparse R–C testing [24,25].

## 2. PSSn ANALYSIS IN GSSM

The definition of PSSn is shown as Eq. (1),

$$\text{PSSn} = \frac{\iint_{A(f_x, f_y)} |\text{OTF}_e|^2 |\text{OTF}_{t+a+e}|^2}{\iint_{A(f_x, f_y)} |\text{OTF}_{t+a+e}|^2}, \tag{1}$$

where $\text{OTF}_e$ is the optical transfer function (OTF) due to error of telescope. $\text{OTF}_{t+a+e}$ is the OTF of telescope under seeing considering the error and seeing. $A(f_x, f_y)$ is the integration area in frequency domain.

For wavefronts with the same RMS but different frequency components, the corresponding far-field diffraction patterns and their PSSn would be different. The relationship between the wavefront frequency component and the PSSn is shown in Fig. 1. Generally, with the increase in internal fluctuation, the PSSn will decrease correspondingly. Moreover, with the rotation of the wavefront, the value of PSSn will change.
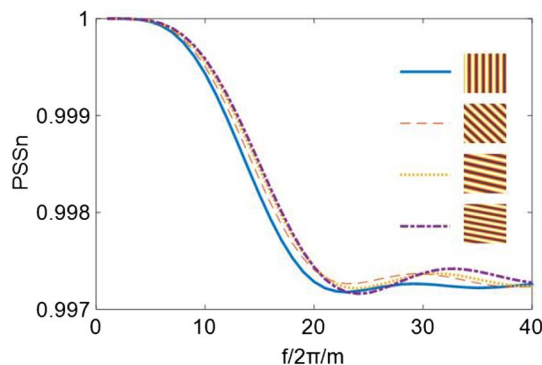
where $\gamma = \frac{\lambda z}{2}$, $P$ is the generalized pupil function, and $\lambda$ is the wavelength. $x, y, z$ is the coordinate, and $f_x, f_y$ is the spatial frequency.

From Eq. (2), it can be inferred that the PSSn of the sparsely sampled case will be less than that of the full-aperture case. The relation between the sparse-aperture sampling ratio and PSSn is shown in Fig. 2. If there is no overlap between subapertures, the limit PSSn is 0.2597.

## 3. RITCHEY–COMMON SPARSE-APERTURE TESTING

The R–C method can realize the testing of an extremely large flat, without requiring a large interferometer. It makes full use of the existing standard spherical mirror, thereby improving the economic efficiency. When combined with a translation or rotation mechanism, the mirror figure of the large flat can be tested. The experimental scheme used for realizing the testing in the R–C sparse method is shown in Fig. 3(a).

A laser tracker, a coordinate measuring machine, can obtain a more precise R–C angle, $\theta$. First, the position of the sphere-mounted retroreflector (SMR) is measured before recording the SMR's coordinate reflected via the planar mirror. By averaging these two coordinates, the position and normal direction of the planar mirror can be obtained. Practically, in order to reduce the error introduced by moving the SMRs, the target SMR position is obtained by averaging the positions of two SMRs placed symmetrically on either side of the target SMR.
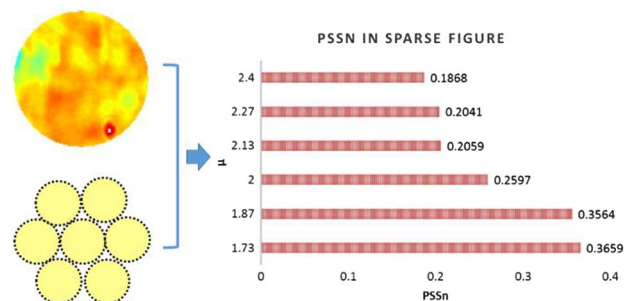


**Fig. 1.** Relationship between wavefront frequency and PSSn.



**Fig. 2.** PSSn limit values of sparse-aperture sampling.
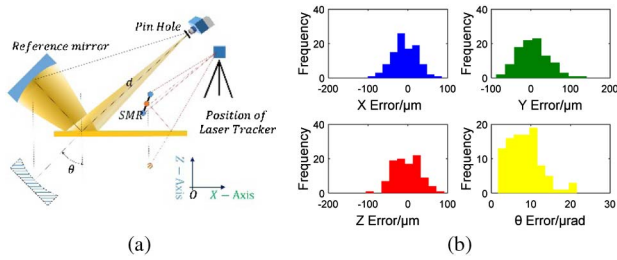
**Fig. 3.** Sketch of Ritchey–Common sparse-aperture testing: (a) coordinate system and details of the assembly and (b) accuracy of $\theta$ testing (at $\theta = 55°$ and $d = 5$ m).

Second, the position of the light source point is determined by the pinhole setting before the interferometer. Then, the laser tracker is adjusted to reflect the light beam onto the planar mirror and the spherical mirror, which is eventually received by the target SMR through the pinhole. We can calculate the exact $\theta$ using the angle and length information. The $\theta$ obtained by this method is not only unique but also accurate because of the direct rebuilding of the main light path. The position accuracy of the reflection point on the reference sphere and $\theta$ testing accuracy (at $\theta = 55°$ and $d = 5$ m) are shown in Fig. 3(b).

The R–C sparse-aperture testing needs to realize the relay transformation of the wavefront. In the measurement process, we need to consider the interconversions among the following coordinate systems: (i) the interferometer coordinate system for measuring each subaperture; (ii) the mirror local coordinate system; and (iii) the coordinate system of the whole planar mirror.

The relationship between the physical coordinates and pupil coordinates can be established using targets. Practically, there are many targets on a planar mirror under test, and the corresponding areas will appear on the measurement data matrix.

After obtaining the surface figure, we can use Eq. (2) to calculate the OTF and PSSn. The shape of the reference spherical mirror's projection on the planar mirror is elliptical in this testing; therefore, it can be considered suitable to process the GSSM figure measurement.

A preliminary sparse-aperture measurement process of a planar mirror is processed as shown in Fig. 4 (at $\theta = 55°$). The resultant PSSn is 0.3766 and the corresponding sparse-aperture PSSn obtained by the planar interferometer is 0.3693.
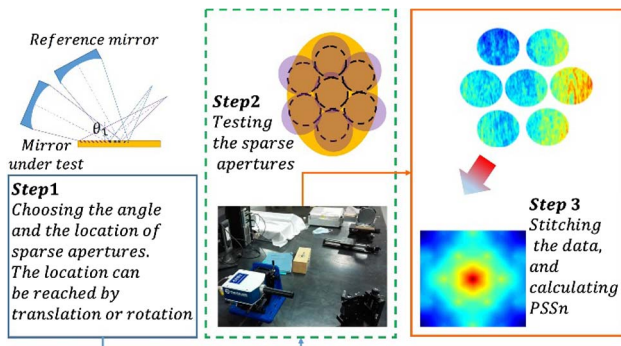
## 4. TESTING ERROR ANALYSIS

To understand the testing results of the RC sparse testing better, an error analysis is necessary. The metrological errors of the sparse-aperture R–C method can be classified into in-plane errors and out-of-plane errors. In-plane errors refer to the errors due to the translation and rotation of the sparse apertures. Meanwhile, the out-of-plane errors are the errors perpendicular to the direction of the GSSM's norm line.

### A. In-Plane Error

The in-plane errors include the shifting error and irregularity error. Testing at different angles will suppress the circumferential error, and, hence, it is ignored here [26].

The R–C method requires removing the flat, relative to the reference surface. In this process, even if a target is used, an alignment error (shifting) will be introduced, as shown in Fig. 5(a). Assuming that the interferometer coordinate system is $W(x', y')$ and the mirror coordinate system is $W_P(x, y)$, the following equations [Eqs. (3) and (4)] represent the relationship between the two coordinate systems:

$$W(x', y') = \sum_{u=0}^{U} \sum_{v=0}^{V} a_{uv} x'^{u} y'^{u-v} \tag{3}$$

and

$$W_P(x, y) = 4 \cos \theta \sum_{u=0}^{U} \sum_{v=0}^{V} a_{uv} \left( \frac{x}{\cos \theta} \right)^{u} y^{u-v}. \tag{4}$$

Among them, $a_{uv}$ is a coefficient of polynomials presenting the figure. $U$ and $V$ are integrations referring to the order of polynomials used here. $\theta$ is the R–C angle.

Assuming the alignment error is $\delta$ along the $x$ direction, the shifting error expression is shown in Eq. (5). The effect of the shifting error is shown in Fig. 5(b).

$$W_P(x + \delta, y) - W_P(x, y)$$

$$= 4 \cos \theta \sum_{u=0}^{U} \sum_{v=0}^{V} a_{nm} \sum_{j=0}^{m} C_m^j \left( \frac{x}{\cos \theta} \right)^{m-j} \left( \frac{\delta}{\cos \theta} \right)^{j} y^{n-m}$$

$$- 4 \cos \theta \sum_{u=0}^{U} \sum_{v=0}^{V} a_{nm} \left( \frac{x}{\cos \theta} \right)^{m} y^{n-m}$$

$$= 4 \cos \theta \sum_{u=0}^{U-1} \sum_{v=0}^{V} \frac{a_{nm}}{\cos^m \theta} \sum_{j=1}^{m} C_m^j x^{m-j} \delta^j y^{n-m}. \tag{5}$$

RC sparse testing will project the pupil of the system on the flat surface. Therefore, during this process, the aperture expansion



**Fig. 4.** Preliminary sparse-aperture measurement of planar mirror.
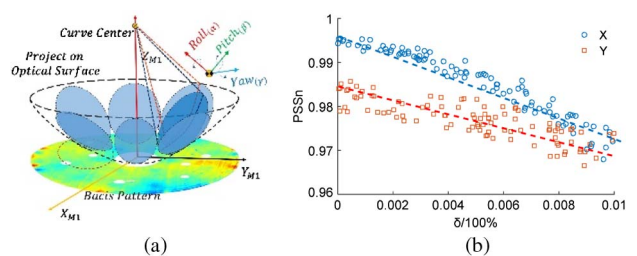


**Fig. 5.** Ritchey–Common sparse-testing in-plane error: (a) coordinate system and (b) effect of shifting error.

(growth), shrinkage, and irregularity of sparse aperture are unavoidable.

An aperture deformation parameterized model was set up as shown in Fig. 6(a). The maximum distance between the edge of the subaperture and the chord *ab* is $h_{max}$. Here, we used $0.99h_{max}$ and $1.01h_{max}$ to simulate the boundary of the subaperture under contraction and expansion. The directions are shown in Fig. 6(b), along with the corresponding PSSn.

## B. Out-of-Plane Error

The out-of-plane errors include the tipping error, tangential/sagittal error, and seeing.

Every sparse aperture detects only a part of the large flat mirror. In a smaller area, the low-order aberrations play a primary role. On the other hand, because of the measurement errors, there is a certain amount of relative piston and tip/tilt errors between the subapertures. The accuracy of the results will be affected greatly if these components are retained.

The PSSn is used as the evaluation criterion, and the rigid-body displacement in the subaperture is removed using the optimized method, as shown in Fig. 7.

The PSSn of the result is estimated first, and the apertures are tipped/tilted randomly. Then, after searching for the maximum PSSn in this data set, the gradient can be estimated by the rigid-body motion of the maximum case. After several steps, the rigid-body displacement in the sparse-aperture R–C testing will be removed to some extent; however, some residual components may be present.

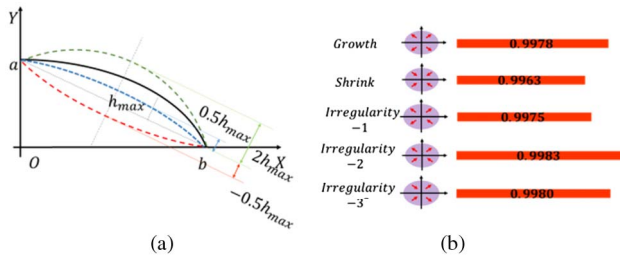We analyze the impact of the individual subaperture rigid-body displacement on the overall PSSn. The impact of the nth

aperture and tip/tilt ($\mathrm{Var}\Phi^S_{x\_n}, \mathrm{Var}\Phi^S_{y\_n}$) on the overall slope RMS is $\mathrm{Var}\Phi^F_n$, as shown in Eq. (6) [27,28]:

$$\mathrm{Var}\Phi^F_n = \mathrm{Var}\Phi^S_{x\_n} \cos^2\left(\frac{2\pi}{N}\right) + \mathrm{Var}\Phi^S_{y\_n} \sin^2\left(\frac{2\pi}{N}\right). \quad \textbf{(6)}$$

The influence of the $N$ subaperture tip/tilt error on the overall slope RMS is given by Eq. (7),

$$\mathrm{Var}\Phi^F = \sum_{n=1}^{N} \mathrm{Var}\Phi^F_n. \quad \textbf{(7)}$$

The PSSn of the ideal system is 1, and with the decrease in this value, the difference between the ideal system and practical system becomes larger. The influence of the $N$ subaperture piston and tip/tilt error on the whole PSSn is shown in Eq. (8),

$$\mathrm{PSSn}_{tipping} = 1 - \mu r_0^2 \left(\frac{2\pi}{\lambda}\right)^2 \frac{\mathrm{Var}\Phi^F}{2\pi^2} = 1 - 2\gamma \frac{\mathrm{Var}\Phi^F}{\lambda^2}, \quad \textbf{(8)}$$

where $\gamma = \mu r_0^2$ and $\gamma = 0.11 \ \mu m/rad$.

For the R–C sparse-aperture testing in subapertures, the primary deformation, which is similar to power, will lead to different imaging positions in the tangential and sagittal directions and introduce additional astigmatism. For GSSM, which has very tight requirements regarding astigmatism, the error in the sag/tan direction will influence the estimation accuracy of astigmatism and its corresponding PSSn. The tangential and sagittal focal plane for R–C sparse-aperture testing is shown in Fig. 8.

Next, we calculate the slope RMS of astigmatism,

$$\Phi_5(x,y) = \alpha_5\rho^2 \cos 2\theta = \alpha_5\rho^2(2\cos^2\theta - 1)$$
$$= 2\alpha_5 x^2 - \alpha_5(x^2 + y^2), \quad \textbf{(9)}$$

where $\alpha_5$ is the astigmatism coefficient. The slopes introduced by astigmatism in both directions are shown in Eq. (10),

$$\Phi^S_{5\_x\_n}(x,y) = \alpha_{5\_n}(4x) - \alpha_5(2x) = 2\alpha_{5\_n}\rho \cos\theta$$
$$\Phi^S_{5\_y\_n}(x,y) = -\alpha_{5\_n}(2y) = -2\alpha_{5\_n}\rho \sin\theta, \quad \textbf{(10)}$$

where $A$ is the area of the subaperture. The mean of Eq. (10) is shown in Eq. (11),



**Fig. 6.** Influence of aperture in-plane error: (a) aperture deformation parameterization model and (b) corresponding PSSn.



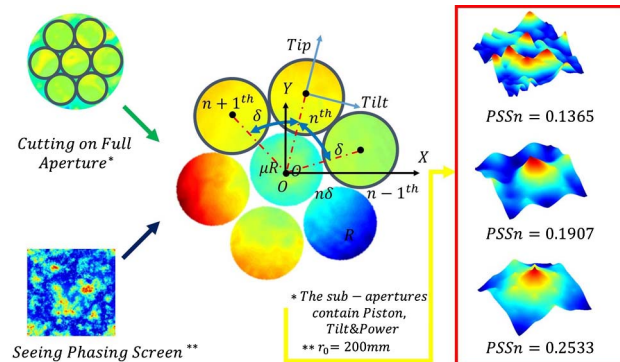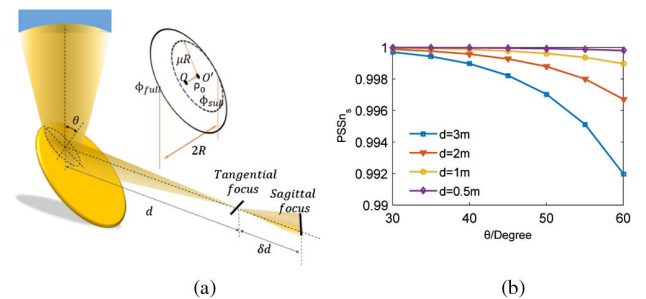**Fig. 7.** Sparse-aperture Ritchey–Common testing rigid-body displacement removal.



**Fig. 8.** Tangential and sagittal error for Ritchey–Common sparse-aperture testing: (a) parameterization model and (b) corresponding PSSn.

$$\langle \Phi^S_{5\_x\_n}(x,y)\rangle = \iint_A 2\alpha_{5\_n}\rho \, \cos\theta \rho \mathrm{d}\theta \mathrm{d}\rho / A$$

$$= \iint_A 2\alpha_{5\_n}\rho^2 \, \cos\theta \mathrm{d}\theta \mathrm{d}\rho / A$$

$$= \frac{2\alpha_{5\_x\_n}}{A} \iint_A \rho^2 \, \cos\theta \mathrm{d}\theta \mathrm{d}\rho = 0$$

$$\langle \Phi^S_{5\_y\_n}(x,y)\rangle = \frac{-2\alpha_{5\_n}}{A} \iint_A \rho^2 \, \sin\theta \mathrm{d}\theta \mathrm{d}\rho = 0. \tag{11}$$

The mean square of Eq. (10) is shown in Eq. (12),

$$\mathrm{Var}\Phi^S_{5\_x\_n} = \iint_A 4\alpha^2_{5\_n}\rho^2 \cos^2\theta \rho \mathrm{d}\theta \mathrm{d}\rho / A$$

$$= \iint_A 4\alpha^2_{5\_n}\rho^3 \cos^2\theta \mathrm{d}\theta \mathrm{d}\rho / A$$

$$= \frac{4\alpha^2_{5\_n}}{A}\frac{\pi R^4}{4} = \frac{\alpha^2_{5\_n}\pi R^4}{A}$$

$$\mathrm{Var}\Phi^S_{5\_y\_n} = \iint_A 4\alpha^2_{5\_n}\rho^3 \sin^2\theta \mathrm{d}\theta \mathrm{d}\rho / A$$

$$= \frac{\alpha^2_{5\_y}\pi R^4}{A}. \tag{12}$$

The influence of the $N$ subaperture sag/tan error on the overall slope RMS is obtained from Eq. (13),

$$\mathrm{Var}\Phi^F_5 = \sum_{n=1}^{N}(\mathrm{Var}\Phi^S_{5\_x\_n} + \mathrm{Var}\Phi^S_{5\_y\_n}), \tag{13}$$

where $R$ is the radius of the full aperture while $\mu$ is the radius of the subaperture proportion, and $\rho_0$ is the polar diameter of the subaperture. The distance between the tangential focal plane and sagittal focal plane is given in Eq. (14). $\theta_{\_n}$ is set as 55°.

$$a_{5\_n} = \frac{16d^2 b_4 \sin^2\theta_{\_n}}{4\mu^2 R^2 \cos\theta_{\_n}}. \tag{14}$$

Here, Eq. (15) declares the relationship between PSSn and the slope RMS.

$$\mathrm{PSSn_{sag/tan}} = 1 - 2\gamma \frac{\mathrm{Var}\Phi^F_5}{\lambda^2} = 1 - 4\gamma \frac{\pi R^4}{\lambda^2 A} \sum_{n=1}^{N} \alpha^2_{5\_n}. \tag{15}$$

## C. Air Turbulence

Another experiment error that needs to be considered is the effect of air turbulence near the mirror. The statistical characteristics of the mirror are not distributed uniformly and are dependent on the physical measurements. The "image motion" method is used to purchase the amount of jitter $\sigma_a$ and the atmospheric coherence length $r_0$. The relationship between these parameters [29] is shown in Eq. (16),

$$r_0 = 3.18 k^{-\frac{6}{5}} D^{-\frac{1}{5}} \sigma_a^{-\frac{6}{5}}. \tag{16}$$

Deliberating the fact that the subapertures are independent of each other, it is conceivable to use the subaperture average information on the spatial domain instead of the sequence analysis on time domain. In other words, the correlation operation is used to estimate the correlation length of the atmosphere, instead of the sequence analysis, and the correlation length is estimated in the spatial domain, which can greatly improve
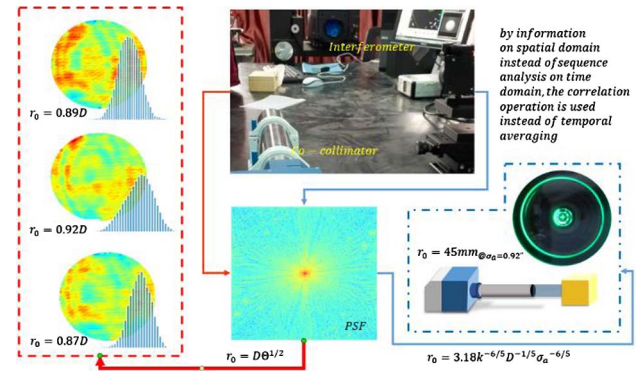


**Fig. 9.** Laboratory seeing measurement.

the real-time function of the measurement is shown in Fig. 9. The aperture average factor [30] is given by Eq. (17),

$$\Theta = \frac{16}{\pi D^2} \int_0^D \rho \mathrm{d}\rho \frac{e^{4C(\rho)}-1}{e^{4C(0)}-1}$$

$$\times \left\{\cos^{-1}\left(\frac{\rho}{D}\right) - \left(\frac{\rho}{D}\right)\left[1 - \left(\frac{\rho}{D}\right)^2\right]^{\frac{1}{2}}\right\}. \tag{17}$$

The relation between the atmospheric coherence length $r_0$, aperture average factor, and aperture $D$ is shown in Eq. (18),

$$r_0 = D\Theta^{\frac{1}{2}}. \tag{18}$$

The influence of the atmosphere on the PSSn is shown in Eq. (19),

$$\mathrm{PSSn_{seeing}} = \int \left| e^{-3.44\left(\frac{\lambda f}{r_0}\right)^{5/3}}\right|^4 \mathrm{d}\vec{f} \Big/ \int \left| e^{-3.44\left(\frac{\lambda f}{r_0}\right)^{5/3}}\right|^2 \mathrm{d}\vec{f}, \tag{19}$$

where $r_0$ is the atmospheric coherence length, $\lambda$ is the wavelength, and $f$ is the spatial frequency. After several calculations, the impact of atmosphere on the PSSn is found to be approximately 0.9974.

As the GSSM is a very large and complicated project, the CIOMP decided to build a 1:4 scaled prototype to learn and understand [31–36]. The cell assembly was accomplished quite recently. The testing error calculation is for the prototype mirror (899 mm × 635 mm). The GSSM prototype will be tested using six sparse apertures of diameter 200 mm. The error
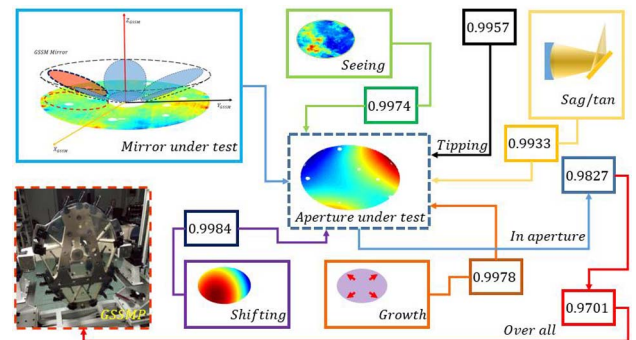


**Fig. 10.** Error analysis in of GSSMP R–C sparse-aperture testing.

analysis of the GSSMP R–C sparse-aperture testing is shown in Fig. 10.

## 5. CONCLUSION

In this study, we investigated the sparse-aperture R–C testing, which is expected to be very useful for the metrology and assembling of GSSMs (TMT's tertiary mirror). The in-plane errors—which include the shifting and irregularity errors—and the out-of-plane errors—which include the tipping error, tangential/sagittal error, and seeing—were analyzed. According to the error analysis, the testing error was 0.9701 for a 1 m scaled planar mirror (GSSMP). Because of the normalized nature of the PSSn, it will be suitable for a 4 m scaled planar mirror (GSSM).

## REFERENCES

1. B. Joseph and J. Houston, "Using the Ritchey–Common test for large plane mirrors (flats)," Opt. Eng. **14**, S-88–90 (1975).
2. K. Shu, "Ray-trace analysis and data reduction methods for the Ritchey-Common test," Appl. Opt. **22**, 1879–1886 (1983).
3. B. Doerband, S. Schulte, F. Schillke, and W. Wiedmann, "Testing large plane mirrors with the Ritchey-Common test in two angular positions," Proc. SPIE **3739**, 330–334 (1999).
4. S. Zhu and X. Zhang, "Ritchey–Common test for a 1.5 m–diameter planar mirror," J. Eur. Opt. Soc. **9**, 14053 (2014).
5. S. Xue, S. Chen, F. Shi, and J. Lu, "Sub-aperture stitching test of a cylindrical mirror with large aperture," Proc. SPIE **9684**, 96840C (2016).
6. N. Samantaray, I. R. Berchera, A. Meda, and M. Genovese, "Realization of the first sub-shot-noise wide field microscope," Light Sci. Appl. **6**, e17005 (2017).
7. S. Wang, D. Su, Y. Chu, X. Cui, and Y. Wang, "Special configuration of a very large Schmidt telescope for extensive astronomical spectroscopic observation," Appl. Opt. **35**, 5155–5161 (1996).
8. S. Yuan, J. Zhang, F. Wang, and X. Liu, "Lateral positioning system for large aperture primary mirror," Opt. Precis. Eng. **25**, 2564–2571 (2017).
9. J. Li, X. Wu, Y. Li, J. Sun, and X. Su, "Position control technology of large aperture mirror based on hydraulic support," Opt. Precis. Eng. **25**, 2599–2606 (2017).
10. W. Luo, Y. Zhang, A. Feizi, Z. Göröcs, and A. Ozcan, "Pixel super-resolution using wavelength scanning," Light Sci. Appl. **5**, e16060 (2016).
11. H. Hu, H. Zhao, Z. Liu, L. Xiao, and X. Zhang, "Hydrostatic support system for in-situ optical testing of a 4 m aperture SiC mirror," Opt. Precis. Eng. **25**, 2607–2613 (2017).
12. F. Yan, B. Fan, X. Hou, and F. Wu, "Absolute subaperture testing by multiage averaging and Zernike polynomial fitting method," Opt. Eng. **52**, 085101 (2013).
13. X. Xu, Z. Shen, G. Tong, and Z. Wang, "Sparse subaperture stitching method for measuring large aperture planar optics," Opt. Eng. **55**, 024103 (2016).
14. S. Chen, Y. Dai, S. Li, X. Eng, and J. Wang, "Error reductions for stitching test of large optical flats," Opt. Laser Technol. **44**, 1543–1550 (2012).
15. V. Bianco, P. Memmolo, M. Paturzo, A. Finizio, B. Javidi, and P. Ferraro, "Quasi noise-free digital holography," Light Sci. Appl. **5**, e16142 (2016).
16. L. Yan, X. Wang, L. Zheng, X. Zeng, H. Hu, and X. Zhang, "Experimental study on subaperture testing with iterative triangulation algorithm," Opt. Express **21**, 22628–22644 (2013).
17. G. Angeli, B. Seo, C. Nissly, and M. Troy, "A convenient telescope performance metric for imaging through turbulence," Proc. SPIE **8127**, 812709 (2011).
18. T. Zhao, Y. Qiao, N. Sun, and J. Xie, "Surface deformation of theodolite primary mirror under the support system," Chin. Opt. **10**, 477–483 (2017).
19. Y. Zheng, J. Bian, X. Wang, J. Liu, P. Feng, H. Ge, O. Martin, and W. Zhang, "Revisiting Newton's rings with a plasmodia optical flat for high-accuracy surface inspection," Light Sci. Appl. **5** e16156 (2016).
20. Z. Zhao, H. Zhao, F. Gu, H. Du, and K. Li, "Non-null testing for aspheric surfaces using elliptical sub-aperture stitching technique," Opt. Express **22**, 5512–5521 (2014).
21. S. Pechprasarn, B. Zhang, D. Albutt, J. Zhang, and M. Somekh, "Ultrastable embedded surface plasmon confocal interferometry," Light Sci. Appl. **3**, e187 (2014).
22. S. Dong, K. Guo, X. Li, H. Chen, and D. Zhang, "Design and analysis of adjustment mechanism with slit diaphragm flexures for optical elements," Chin. Opt. **10**, 790–797 (2017).
23. X. Yang, B. Gao, and X. Cui, "New application of stitching interferometry by using Ritchey-Common method for testing the large aperture optical flat," Opt. Tech. **31**, 611–613 (2005).
24. B. Seo, C. Nissly, M. Troy, G. Angeli, R. Bernier, L. Stepp, and E. Williams, "Estimation of normalized point-source sensitivity of segment surface specifications for extremely large telescopes," Appl. Opt. **52**, 4111–4122 (2013).
25. B. Seo, C. Nissly, G. Angeli, B. Ellerbroek, J. Nelson, N. Sigrist, and M. Troy, "Analysis of normalized point source sensitivity as a performance metric for large telescopes," Appl. Opt. **48**, 5997–6007 (2009).
26. E. Christopher and R. Kestner, "Test optics error removal," Appl. Opt. **35**, 1015–1021 (1996).
27. G. Smith and J. Burge, "Subaperture stitching tolerancing for annular ring geometry," Appl. Opt. **54**, 8080–8086 (2015).
28. S. Chen, S. Li, and G. Wang, "Subaperture test of wavefront error of large telescopes: error sources and stitching performance simulations," Proc. SPIE **9298**, 929817 (2014).
29. E. Silbaugh, B. Welsh, and M. Roggemann, "Characterization of atmospheric turbulence using wavefront slope measurements," Proc. SPIE **2828**, 210–220 (1996).
30. N. Perlot and D. Fritzsche, "Aperture averaging: theory and measurements," Proc. SPIE **5338**, 233–242 (2004).
31. Q. An, J. Zhang, F. Yang, H. Zhao, and W. Liang, "Performance improvement of the Giant Steerable Science Mirror prototype: calibration, added-on damping treatment, and warping harness," Appl. Opt. **56**, 10009–10015 (2017).
32. F. Yang, H. Zhao, P. Guo, Q. An, and H. Jiang, "Pre-construction of giant steerable science mirror for TMT," Proc. SPIE **9573**, 95730T (2015).
33. Q. An, J. Zhang, F. Yang, and H. Zhao, "Normalized point source sensitivity analysis in GSSM prototype," Chin. Opt. Lett. **15**, 111202 (2017).
34. F. Yang and Q. An, "The evaluation and analysis of mirror seeing based on PSSn," Opt. Precis. Eng. **24**, 979–985 (2016).
35. F. Yang, Q. An, J. Zhang, H. Zhao, P. Guo, and H. Jiang, "Seeing metrology of large aperture mirror of telescope," Opt. Precis. Eng. **25**, 2572–2579 (2017).
36. L. Han, J. Zhang, F. Yang, and Q. An, "Estimation of the GSSM calibration error," Appl. Opt. **55**, 8884–8892 (2016).